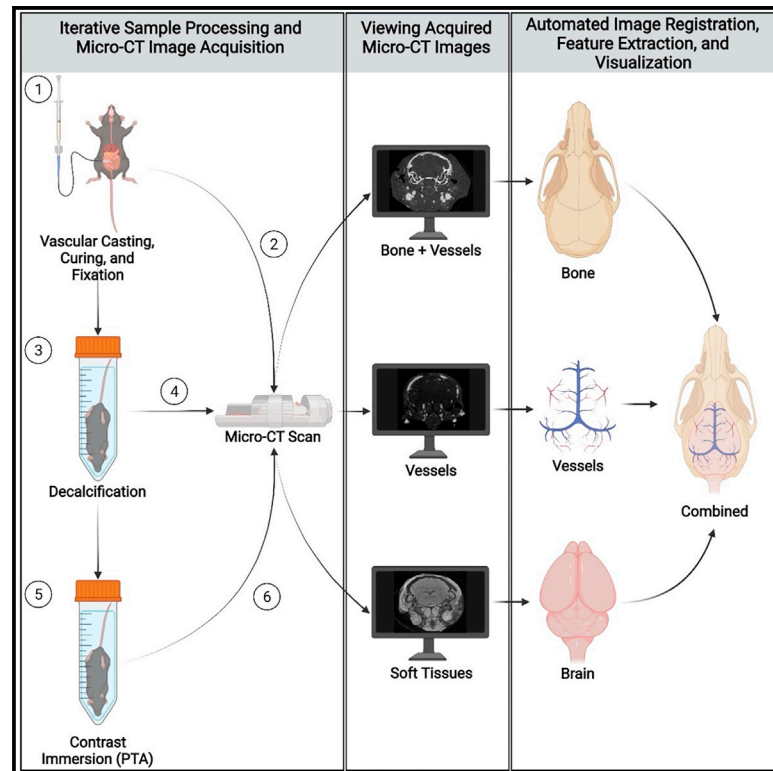**Report**

Non-invasive *in situ* visualization of the murine cranial vasculature

Graphical abstract

Authors

Jared S. Rosenblum,
Anthony J. Cappadona,
Pashayar P. Lookian, ..., John D. Heiss,
Karel Pacak, Zhengping Zhuang

Correspondence

zhengping.zhuang@nih.gov (Z.Z.),
jared@neurosimplicity.com (J.S.R.)

In brief

Rosenblum et al. develop a method and system to visualize the entire *in situ* cranial vasculature and surrounding anatomy. The authors combine vascular casting with iterative sample processing and image acquisition with automated image registration, feature extraction, and visualization.

Highlights

- Vascular casting and micro-CT allow visualization of vascular anatomy

- Non-invasive visualization of *in situ* cranial vasculature and surrounding anatomy

- Non-destructive iterative sample processing allows repeated image acquisition

- Tools for automated image processing, feature extraction, and visualization

CellPress

Report

Non-invasive *in situ* visualization
of the murine cranial vasculature

Jared S. Rosenblum,[2,10,11,*] Anthony J. Cappadona,[1,10] Pashayar P. Lookian,[1,10] Vikram Chandrashekhar,[2]
Jean-Paul Bryant,[3] Vibhu Chandrashekhar,[2] David Y. Zhao,[4] Russell H. Knutsen,[5] Danielle R. Donahue,[6]
Dorian B. McGavern,[7] Beth A. Kozel,[5] John D. Heiss,[3] Karel Pacak,[8] and Zhengping Zhuang[1,*]

[1]Neuro-Oncology Branch, National Cancer Institute, National Institutes of Health, Bethesda, MD 20892, USA
[2]NeuroSimplicity LLC, Rockville, MD 20852, USA
[3]Surgical Neurology Branch, National Institute of Neurological Disorders and Stroke, National Institutes of Health, Bethesda, MD 20892, USA
[4]Department of Neurosurgery, Medstar Georgetown University Hospital, Washington, DC 20007, USA
[5]Laboratory of Vascular and Matrix Genetics, National Heart Lung and Blood Institute, National Institutes of Health, Bethesda, MD 20892, USA
[6]Mouse Imaging Facility, National Institute of Neurological Disorders and Stroke, National Institutes of Health, Bethesda, MD 20892, USA
[7]Viral Immunology and Intravital Imaging Section, National Institute of Neurological Disorders and Stroke, National Institutes of Health, Bethesda, MD 20892, USA
[8]*Eunice Kennedy Shriver* National Institute of Child Health, National Institutes of Health, Bethesda, MD 20892, USA
[10]These authors contributed equally
[11]Lead contact
*Correspondence: zhengping.zhuang@nih.gov (Z.Z.), jared@neurosimplicity.com (J.S.R.)
https://doi.org/10.1016/j.crmeth.2021.100151

MOTIVATION The entire intact murine cranial vasculature has not yet been visualized. Understanding normal cerebrovascular anatomic relationships is critical to the study of intracranial pathologies. Current *in vivo* contrast-based imaging methods for mice, such as micro-computed tomography (micro-CT) or magnetic resonance imaging (MRI), are limited in resolution of fine vasculature due to motion artifact and inadequate contrast filling. Optical sectioning using light-sheet microscopy, which is a high-resolution *ex vivo* alternative for imaging the brain, can resolve fine cerebrovasculature but cannot presently be performed on the whole head with the skull intact while preserving the sample for further investigation. Here, we developed a workflow to non-invasively and non-destructively generate high-resolution maps of the murine whole-head vasculature and the surrounding anatomy by using terminal vascular polymer casting, iterative sample processing, and high-resolution *ex vivo* micro-CT.

SUMMARY

Understanding physiologic and pathologic central nervous system function depends on our ability to map the entire *in situ* cranial vasculature and neurovascular interfaces. To accomplish this, we developed a non-invasive workflow to visualize murine cranial vasculature via polymer casting of vessels, iterative sample processing and micro-computed tomography, and automatic deformable image registration, feature extraction, and visualization. This methodology is applicable to any tissue and allows rapid exploration of normal and altered pathologic states.

INTRODUCTION

Our understanding of central nervous system function during states of health and disease depends critically on our ability to generate detailed and accurate anatomic maps of the entire vascular network that supplies this compartment. The translational study of cranial murine disease models requires a standardized visualization method that contextualizes the entire vasculature *in situ* relative to the surrounding anatomy, which has yet to be accomplished and would greatly advance our understanding of neurovascular interfaces (Dorr et al., 2007;

Walker et al., 2011; Ghanavati et al., 2014; Choi et al., 2017; Xiong et al., 2017; Rindone et al., 2021; Cai et al., 2019). *In vivo* contrast-based angiography is standard for defining these relationships in living larger animals and humans (Grossberg et al., 2019). However, due to low resolution and artifacts of *in vivo* image acquisition in mice, it is difficult to image and visualize cranial vasculature as it interfaces with related functional tissues, such as the brain, meninges, and skull (Badea et al., 2008).

As an alternative to *in vivo* contrast-based angiography, casting of vessels with radio-dense polymers has traditionally been
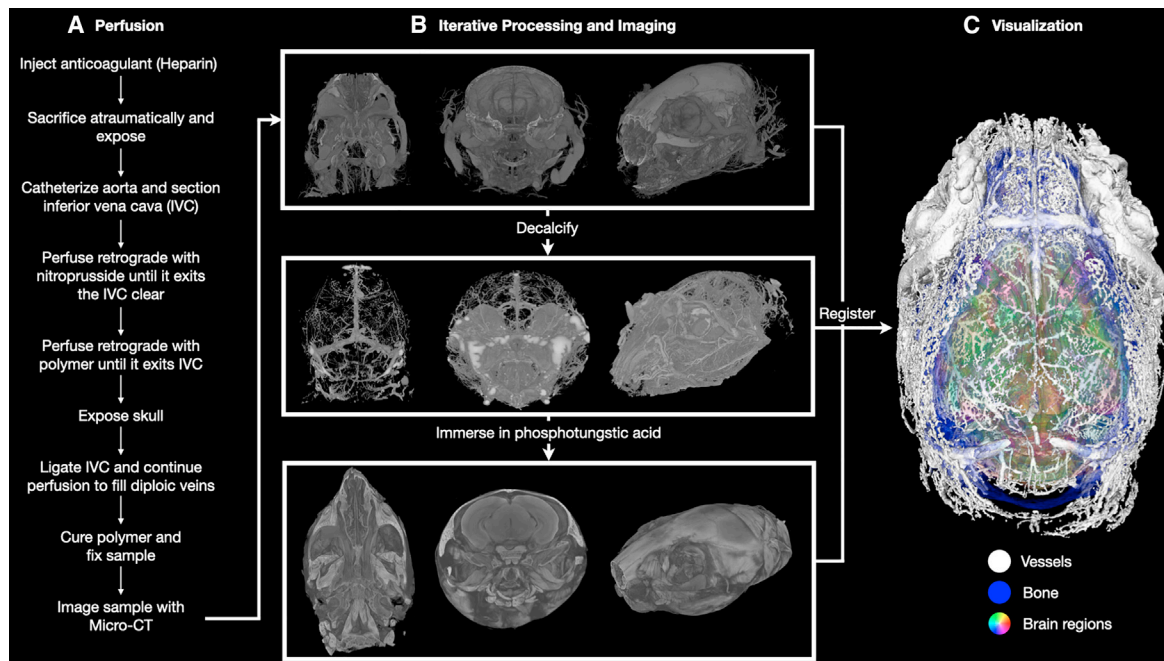
Figure 1. Overview of low-density polymer vascular casting, imaging, and 3D visualization

(A) Steps for cranial vascular casting perfusion are shown.

(B) Iterative sample processing and imaging. The same representative wild-type mouse sample is shown. The top row shows a 3D reconstruction of a whole head micro-CT with Microfil polymer-casted cranial vasculature and bone. Micro-CT after decalcification shown in the middle row highlights the vasculature in isolation. Immersion in phosphotungstic acid (PTA) makes the tissues radio-opaque, as shown in the bottom row.

(C) 3D visualization of all datasets deformably registered to the same space displaying the segmented vessels (white), bone (blue), and brain regions derived from the Allen Reference Atlas Common Coordinate Framework version 3 (multi-color).

combined with tissue or organ dissection, digestion, and dye immersion, along with *ex vivo* image acquisition (Walker et al., 2011; Ghanavati et al., 2014; Knutsen et al., 2020; Christoffersonm and Nilsson, 1988). Typically, high-density, radio-opaque polymer mixtures used in these methods are not optimized for arterio-venous transit, which limits their use to casting of either the arterial or venous system (Knutsen et al., 2020). Conversely, low-density radio-opaque polymers that cross capillary beds are not well visualized in imaging methods such as micro-computed tomography (micro-CT) without prior isolation of the tissue and clearing or digestion, which can distort and/or destroy the gross or fine anatomy of the vasculature (Choi et al., 2017; Hildebrand, 1968; Hong et al., 2020). In addition, these methods are limited by destruction of the sample tissue, limited perfusion, or inadequate visualization. Although newer tissue clearing and immunostaining immersion-based visualization techniques, such as clear lipid-exchanged anatomically rigid imaging/immunostaining-compatible tissue hydrogel (CLARITY) and light-sheet microscopy, provide very high resolution, three-dimensional (3D), intact images, these methods may produce artifacts such as tissue deformation and illumination inhomogeneity (Chung and Deisseroth, 2013; Renier et al., 2014; Lee et al., 2021). Furthermore, these techniques still require dissection and removal of the brain, which can distort the anatomy and precludes the study of the entire cranial vasculature. While advances in tissue clearing and light-sheet microscopy have made it possible to image vasculature within bone or to survey large intact regions of

mice for specific anatomic structures of interest (Cai et al., 2019; Rindone et al., 2021), the processing in these methods requires specific considerations for downstream investigations such as histology, immunohistochemistry, and molecular genetic techniques, among others (Lai et al., 2018).

To visualize the entire murine *in situ* cranial vasculature in relation to the surrounding anatomy and preserve the sample for further investigation, we developed a non-invasive, non-destructive visualization method combining 1) low-density polymer casting with arterio-venous transit, 2) iterative sample processing and micro-CT, and 3) automatic deformable registration and 3D visualization through the Neurosimplicity Imaging Suite. This workflow allowed us to non-invasively construct a high-resolution 3D map of murine cranial vasculature in relation to the brain, surrounding skull bone, and soft tissues.

RESULTS

Overview of our workflow for visualization of cranial vasculature

Figure 1 shows an overview of our approach to visualizing the murine cranial vasculature (see STAR Methods section for details). To ensure capillary transit, we first injected the anticoagulant heparin and allowed the mouse to ambulate before atraumatic sacrifice. We then exposed and catheterized the descending aorta, sectioned the inferior vena cava (IVC), and perfused sodium nitroprusside retrograde through the aorta until
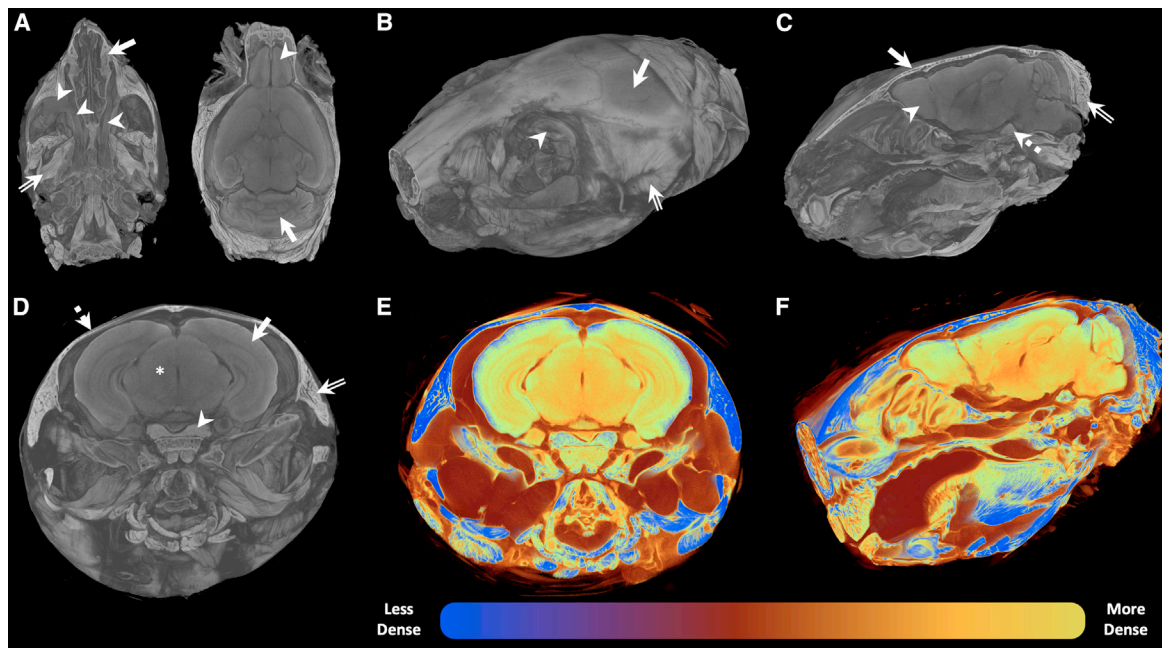
Figure 2. Volumetric rendering of micro-CT of wild-type murine head following polymer perfusion and PTA immersion

(A) Left: Axial plane of micro-CT through the skull base of the whole murine head allows visualization of soft tissue such as muscle (double-lined arrow), bone (arrow), and venous sinuses (arrowhead). Right: The brain is seen in a superior axial plane. Areas of the brain that can be lost or damaged during isolation such as the olfactory bulbs (arrowhead) and cerebellum (arrow) are seen intact with this *in situ* visualization.

(B) Oblique sagittal view of the same sample demonstrates visualization of the retro-orbital sinus (arrowhead), bone matrix (arrow), and muscle (double-lined arrow).

(C) Oblique sagittal view of the same sample shows bone matrix (arrow), brain (arrowhead), and muscle (double-lined arrow). The pituitary gland is also visualized (dashed arrow).

(D) Coronal section of the same sample shows cortex (arrow), midbrain (asterisk), pituitary gland (arrowhead), soft tissues such as muscle (double-lined arrow), and bone (dashed arrow).

(E and F) Coronal (E) and oblique (F) sagittal sections of the same sample with a transfer function specific for the tungsten component of PTA, courtesy of Micro Photonics Inc. (Allentown PA), applied demonstrates the relative radio-density of each tissue type as determined by PTA binding of protein. Brain (yellow) is the most radio-dense, whereas muscle and bone (blue) are the least radio-dense following decalcification. The color bar demonstrates the range of densities assigned to each color by the transfer function.

it exited the IVC. This step cleared blood from and maximally dilated all vessels. Next, we perfused a low-density, radio-opaque polymer through the same catheter until it exited the IVC. Finally, we ligated the IVC, exposed the skull to visualize the diploic veins, and continued perfusion until they were visibly filled. This served as the end point for intracranial filling of vessels.

Following curing and fixation, we processed and imaged the sample via micro-CT at three stages to specifically capture the vascular cast, bone, and soft tissues. We acquired an initial micro-CT before decalcification that shows bone and the vascular cast. We subsequently decalcified the sample to make bone radiolucent and then acquired a second micro-CT. This reveals diploic and emissary vessels within the bone and increases the visibility of intracranial vessels. Finally, we immersed the sample in phosphotungstic acid (PTA), which binds protein in a concentration-dependent manner and makes all tissues visible on a third acquired micro-CT (Figure 2) (Quintarelli et al., 1971; Micro Photonics, 2016). The acquired micro-CT data and the appropriate atlas—in this case the Allen Reference Atlas Common Coordinate Framework Version 3 (ARA CCFv3) (Wang et al.,

2020)—are then deformably registered to the same coordinate space; features of interest including annotated brain regions, bone, and vessels are automatically extracted and visualized in 3D by the Neurosimplicity Imaging Suite.

Iterative processing steps are validated by micro-CT

Multiple micro-CT image datasets were acquired on the same sample following iterative processing to allow the visualization of specific anatomic features including vessels, bone, brain, and other soft tissues. We utilized micro-CT following each step to determine successful processing, such as complete decalcification and diffusion of PTA. Examples of micro-CT images used to determine successful iterative processing are shown in Figure S1.

Acquired micro-CT is registered and visualized together using the Neurosimplicity Imaging Suite

With these three datasets, we then deformably registered the first micro-CT image with bone and vessel to the image of the decalcified sample (Figure 3A). We also registered the micro-CT image following PTA immersion to the image of the decalcified
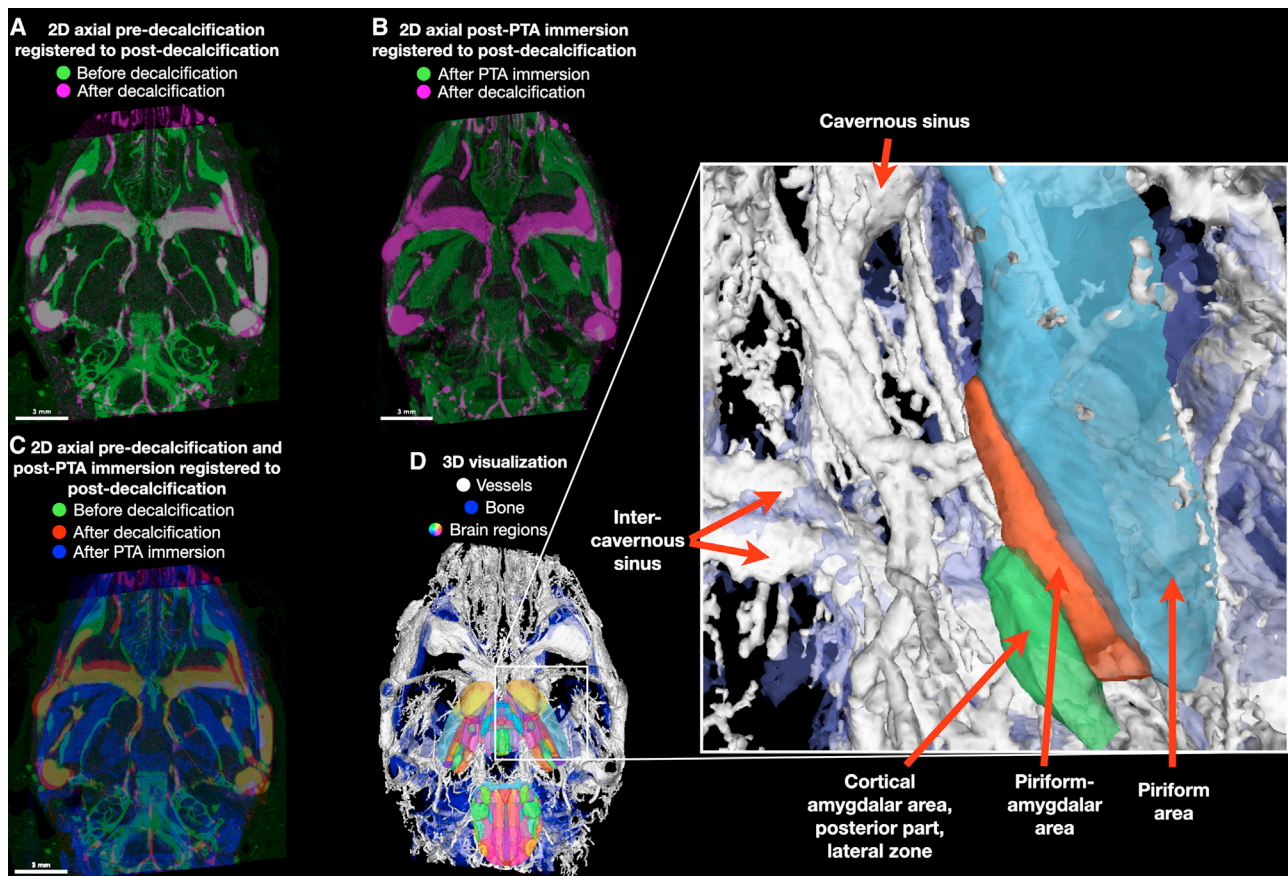
Figure 3. Deformable registration of iteratively processed sample imaged with micro-CT

All the images are reconstructions of the same sample in the axial plane. The scale bars in (A)–(C) represent 3 mm.

(A) 2D axial view of deformably registered raw data from the pre-decalcification (green) and post-decalcification (magenta) registrations. Regions in white are where the two images overlap.

(B) 2D axial view of the post-PTA-immersion (green) and post-decalcification (magenta) registrations. In the PTA raw registration data, vessels are dark; thus, no regions of white are seen.

(C) 2D axial view of the registered raw data from the pre-decalcification (green), post-decalcification (magenta), and post-PTA-immersion (blue) images. Regions in white are where the three images overlap.

(D) Once the raw data are registered to each other, we create a 3D visualization of the *in situ* anatomic relationships of vessels, bone, soft tissue, and brain parenchyma in the same murine sample. The inset shows vessels at the murine skull base going to selected brain nuclei.

sample (Figure 3B). Finally, we registered and displayed all three of these scans in the same space (Figure 3C). This allowed us to visualize the segmented vessels, brain regions, and surrounding anatomy in 3D (Figure 3D, Video S1).

Iterative micro-CT images enable quantification of vessels

We measured the length and diameters of the basilar arteries in a representative set of 10 mice (5 wild type, 5 mutant) prepared and imaged following our method (Table 1); an example measurement is shown in 2D and 3D in Figure 4. Measurements of the total length of the basilar artery are provided in both wild-type and mutant mice (Table 1); mean and standard deviation are given. The diameters of the basilar artery at each anatomic segment (B1, B2, and B3) as defined by junction or takeoff of vessels, e.g., the vertebral arteries or the anterior inferior cerebellar arteries, are also provided; mean and standard deviation

are given. Comparison of basilar artery length and diameter at each segment between mutant and wild-type mice revealed no significant difference in total length or diameter of the B1 segment but a significant difference in the diameters of the B2 and B3 segments (p value <0.05).

DISCUSSION

To evenly cast all the vessels in the head, we developed a method of systemic low-density polymer perfusion. Low-density Microfil has been shown to be superior to other contrast agents in perfusion of both the intracranial arterial and the venous vasculature (Hong et al., 2020). We modified this previously described method in three important ways. 1) We used a lower-density polymer mixture to ensure non-destructive capillary transit; 2) we perfused retrograde through the descending aorta to ensure even filling of the anterior and posterior cranial

Table 1. Quantitative measurement of basilar artery length and segment diameter in wild-type mice and *EPAS1*-gain-of-function mutation mouse model

Type	WT	WT	WT	WT	WT	M	M	M	M	M
Total basilar length (μm)	4,494	5,123	4,245	4,188	4,376	4,739	4,743	4,564	4,577	4,008
B1 segment diameter (μm)	229	170	135	170	101	104	153	175	180	95
B2 segment diameter (μm)	199	195	183	189	187	176	149	169	176	109
B3 segment diameter (μm)	192	147	131	138	151	89	125	134	139	88
Average length (μm)	4,485 ± 376					4,526 ± 302				
Average diameter B1 (μm)	161 ± 48					141 ± 40				
Average diameter B2 (μm)	191 ± 6					156 ± 28				
Average diameter B3 (μm)	152 ± 24					115 ± 25				

WT, wild-type samples; M, mutant samples. Length and diameter measurements were made using the line annotation tool in Neurosimplicity Imaging Suite. Total length of the basilar artery and diameters of its three main segments are provided in microns (μm) for each sample along with averages and standard deviations for each measurement. The B1 segment of the basilar artery includes the region from its origin at the vertebral arteries to the origin of anterior inferior cerebellar arteries. The B2 segment of the basilar artery includes the region from the takeoff at the anterior inferior cerebellar arteries to the origin of superior cerebellar arteries. The B3 segment of the basilar artery includes the region from its takeoff at the superior cerebellar arteries to the origin of the posterior cerebral arteries.

circulation; and 3) we created a closed system to allow for backfilling of the venous vasculature of the entire head. Although other polymers can be optimized for arterio-venous transit (Hlushchuk et al., 2020), we chose Microfil polymer because others such as vinylite have unfavorable polymerization and curing properties, including expansion and heat release, that may damage fine vasculature (Hildebrand, 1968; Merill, 1940). Our perfusion method, when combined with micro-CT, showed the major cranial vessels in relation to the skull. However, visualization of finer intracranial vasculature was limited by the presence of the radio-dense skull. Furthermore, vascular interfaces with bone and soft tissues such as brain, which are not inherently radio-dense on micro-CT, were not visible.

We developed an iterative sample processing and micro-CT approach to visualize the vessels within bone and neurovascular interfaces. Following our first round of micro-CT to visualize cranial bone and polymer-casted vessels, we then decalcified the same sample and repeated micro-CT to generate an image of the isolated cranial vasculature. From this decalcified scan, we were able to automatically render a segmentation of the *in situ* cranial vasculature separated from bone. Next, we immersed the same sample in PTA and performed a third round of micro-CT to generate an image containing bone, vessels, and soft tissue. We then automatically and deformably registered all three scans and the Allen Reference Atlas brain region annotations into the same space and extracted features of interest for visualization of the brain, bone, and vessels in using the Neurosimplicity Imaging Suite.

Using only the first round of the workflow described above, we had previously characterized abnormalities in cranial vasculature and surrounding bone in a mouse model of Pacak-Zhuang syndrome (Figure S2) (Rosenblum et al., 2020, 2021). Through our clinical investigations of patients with this syndrome, we recognized that the vascular malformations in these patients are primarily venous and involve both vessels of the brain and the rest of the head (Rosenblum et al., 2021). However, without further sample processing we could not visualize neurovascular interfaces with casting and micro-CT alone. Thus, we developed a non-invasive, non-destructive iterative sample processing and micro-CT workflow that allowed us to visualize vessels, soft tissue, and bone separately. The acquired data can be converted to Hounsfield units, a commonly used linear rescaling, if samples of water and air are also acquired with the same parameters on the same machine (Figure S3). Quantitative analysis and measurements, however, can be performed on the acquired data, which are measured in attenuation, because the relative densities of regions within the sample are still the same. Herein, we provide an example of quantification that can be performed using our method by measuring the lengths and diameters of the basilar arteries in wild-type mice and the mouse model of *EPAS1*-Gain-of-Function syndrome, which revealed that the mutant B2 and B3 segments of the basilar artery were significantly smaller than those of the wild type.

Our workflow, when combined with the registration and 3D visualization, offers an unprecedented understanding of the anatomy, particularly neurovascular interfaces. Although significant advances allowing imaging of vasculature in bone and evaluation of structures of interest over large intact regions of mice have recently been made in tissue clearing and light-sheet microscopy (Rindone et al., 2021; Cai et al., 2019), these methods are still limited in visualizing all of the structures within the entire intact head, e.g., brain parenchyma, bone, and vessels. Moreover, while these methods are destructive and preclude further downstream investigation using standard methods such as histology, immunohistochemistry, and molecular genetic techniques, our approach preserves the sample of these further investigations. Since the vasculature is not perfused with fixative in our casting method, fixation parameters can be chosen and
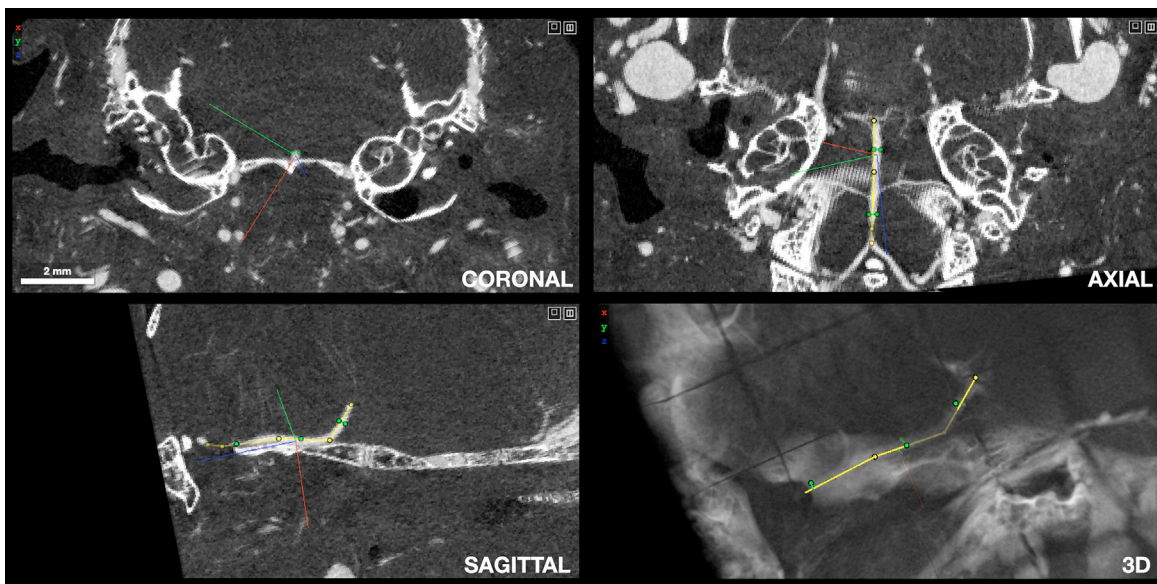
Figure 4. Representative measurements of the basilar artery in micro-CT images of murine whole-head before decalcification
A four-panel visualization of a representative micro-CT of a polymer-perfused wild-type mouse, including coronal, axial, sagittal, and 3D views. The yellow lines indicate the measured length of the basilar artery; the green lines perpendicular to the previously mentioned yellow lines indicate the measured diameters of the different segments of the basilar artery. All measurements and visualizations were performed in Neurosimplicity Imaging Suite. The scale bar in the top left applies to all 2D slices and represents 2 mm.

optimized for additional tissue studies. The high-resolution *in situ* visualization afforded by this non-invasive, non-destructive approach should also aid future studies focused on analyzing regions of interest, such as specific neurovascular interfaces.

Previous studies have generated incredible maps of cerebrovasculature at high resolution by combining optical methods such as light-sheet microscopy with tissue-clearing methods. For example, Kirst et al. recently presented a tremendous resource for understanding cerebrovasculature (Kirst et al., 2020). However, the methods used in this study required isolation of the brain from the bone and surrounding tissues. Recent advances in this methodology, as mentioned, now allow visualization of vasculature within bone or evaluation of anatomy of interest over large regions of mice by using light-sheet microscopy (Rindone et al., 2021; Cai et al., 2019); however, these techniques still have unique sample preparation considerations for optimizing visualization of multiple markers of interest using antibody-based labeling and allowing for further downstream use of the sample. Our workflow, which is non-invasive and non-destructive, utilizes polymer to cast and define vessels and PTA to bind protein in all tissues in a concentration-dependent manner. These two non-specific methods of labeling tissues, therefore, allow visualization of all structures within the head without removal of the brain. This method therefore allows study of the entire intact cranial vasculature. In addition, by iteratively processing and imaging the same sample, our method can visualize the interfaces of the vasculature with regions of tissues of interest in an unprecedented manner.

Using the Neurosimplicity Imaging Suite, a tool for automated deformable image registration, feature extraction, and visualization, we can combine our iteratively processed samples such

that brain, bone, and vessels from the same sample can all be visualized in the same coordinate space. This software can handle raw data files including bitmap, TIF, and DICOM. Furthermore, we used this tool to automatically register the images from our sample to the anatomic parcellations of the ARA CCFv3, allowing brain-region-level annotation; any other reference atlas could be used. Micro-CT not only allows us to have intact, non-invasive, non-destructive visualization of the whole sample but also, with further optimization of parameters and newer micro-CT machines, allows us to achieve even higher resolution than what we present here.

In conclusion, we have developed a non-invasive, non-destructive approach for visualizing the *in situ* murine cranial vasculature in its entirety with the surrounding anatomy intact. Our reproducible method improves upon shortcomings of past vascular casting and visualization methods by combining even casting of the entire cranial vasculature, iterative sample processing and micro-CT, and automatic deformable registration, feature extraction, and visualization. This method will allow us to develop 1) a murine cranial vascular reference atlas, 2) analytic parameters derived from this atlas, and 3) objective methods to standardize the evaluation of cranial vascular disease in murine models. The use of this method, which can be applied to any tissue, will allow for the rapid exploration and further understanding of normal and disease states.

Limitations of the study

The method and workflow that we present herein allow the non-invasive, non-destructive visualization of the entire murine cranial vasculature by combining terminal vascular polymer casting, iterative sample processing, and imaging with micro-CT. While this method affords unprecedented visualization of

the vasculature of any organ, it requires sacrifice of the animal. As a result, this method alone cannot obtain dynamic imaging that can show the directionality of blood flow within the vessels. Therefore, our method may be unsuitable for studies that are investigating the dynamics of blood flow. In this case, *in vivo* methods may be preferable. For example, the ultrasound (US) method by Tang et al. achieves velocity-based measurements of directionality of blood flow allowing the determination of artery or vein (Tang et al., 2020). There are also many contrast-based and time-of-flight (TOF) MRI methods that enable visualization of the cerebrovasculature in mice (Fouquet et al., 2020; Pastor et al., 2017). Both *in vivo* and *ex vivo* methods have limitations on quantitative evaluation of vasculature such as measurement of vessel diameter. The provision of anesthesia for *in vivo* methods alters cerebral vasodilation and vasoconstriction (Dagal and Lam, 2009; Slupe and Kirsch, 2018). In our *ex vivo* method, we perfuse with sodium nitroprusside to maximally dilate and clear blood from all vessels. While this maximal dilation alters baseline physiologic vasculature, we opt for a uniform effect of vasodilation as opposed to unpredictable combinatorial effects of different anesthetic agents. In mouse models where sodium nitroprusside activity may be altered or affect the condition under study (Liao et al., 2021; Venturelli et al., 2018; Merlini et al., 2017), we would recommend using other vasodilators to achieve the desired effect.

Our workflow is particularly suited for morphological, structural, and developmental studies of vasculature and surrounding anatomy. Although direct comparisons of certain vascular metrics, such as vessel diameter, may not be comparable between our *ex vivo* method and existing *in vivo* methods, comparison of the anatomy can be made. For example, using just our vascular casting method, we identified vascular malformations in a mouse model of Pacak-Zhuang syndrome that recapitulated findings in the *in vivo* human studies (Rosenblum et al., 2020, 2021) (Figure S2). Furthermore, our workflow is not restricted to cranial tissue and can be applied to any organ or tissue of interest to perform similar analyses.

STAR★METHODS

Detailed methods are provided in the online version of this paper and include the following:

- KEY RESOURCES TABLE
- RESOURCE AVAILABILITY
  - Lead contact
  - Materials availability
  - Data and code availability
- EXPERIMENTAL MODEL AND SUBJECT DETAILS
  - Animals
- METHOD DETAILS
  - Vascular perfusion and casting
  - Iterative sample processing and micro-CT image acquisition
  - Optimizing micro-CT parameters
  - Image processing
  - Troubleshooting
- QUANTIFICATION AND STATISTICAL ANALYSIS

AUTHOR CONTRIBUTIONS

J.S.R. conceived the study, developed, and optimized the method; performed experiments; analyzed data; wrote the original manuscript; and revised the manuscript. A.J.C. and P.P.L. performed experiments, analyzed data, and revised the manuscript. Vikram Chandrashekhar conceived the study, developed and optimized the methods, performed experiments, analyzed data, wrote the original manuscript, and revised the manuscript. R.K. developed and optimized the method, performed experiments, analyzed data, and revised the manuscript. D.R.D. helped develop and optimize the method, performed experiments, analyzed data, and revised the manuscript. J.P.B. wrote the original manuscript, analyzed data, and revised the manuscript. D.Z. analyzed data and revised the manuscript. Vibhu Chandrashekhar conceived the study, analyzed data, and revised the manuscript. D.B.M. analyzed data and revised the manuscript. B.A.K. analyzed data and revised the manuscript. J.D.H. analyzed data and revised the manuscript. Z.Z. and K.P. supervised the study, analyzed data, and revised the manuscript.

DECLARATION OF INTERESTS

J.S.R., Vikram Chandrashekhar, and Vibhu Chandrashekhar are affiliated with NeuroSimplicity, LLC, which is a medical device and technology company focusing on medical image processing. The content of this manuscript does not necessarily reflect the views, policies, or opinions of the U.S. Department of Health and Human Services. The mention of commercial products, their source, or their use in connection with material reported herein is not to be construed as an actual or implied endorsement of such products by the United States government.

REFERENCES

Badea, C.T., Drangova, M., Holdsworth, D.W., and Johnson, G.A. (2008). In vivo small-animal imaging using micro-CT and digital subtraction angiography. Phys. Med. Biol. *53*, R319–R350.

Cai, R., Pan, C., Ghasemigharagoz, A., Todorov, M.I., Förstera, B., Zhao, S., Bhatia, H.S., Parra-Damas, A., Mrowka, L., Theodorou, D., et al. (2019). Panoptic imaging of transparent mice reveals whole-body neuronal projections and skull–meninges connections. Nat. Neurosci. *22*, 317–327.

Chandrashekhar, V., Tward, D.J., Crowley, D., Crow, A.K., Wright, M.A., Hsueh, B.Y., Gore, F., Machado, T.A., Branch, A., Rosenblum, J.S., et al. (2021). CloudReg: automatic terabyte-scale cross-modal brain volume registration. Nat. Methods *18*, 845–846.

Choi, J.P., Yang, X., Foley, M., Wang, X., and Zheng, X. (2017). Induction and micro-CT imaging of cerebral cavernous malformations in mouse model. J. Vis. Exp. *127*, 56476.

Christoffersonm, R.H., and Nilsson, B.O. (1988). Microvascular corrosion casting with analysis in the scanning electron microscope. Scanning *10*, 43–63.

Chung, K., and Deisseroth, K. (2013). CLARITY for mapping the nervous system. Nat. Methods *10*, 508–513.

Dagal, A., and Lam, A.M. (2009). Cerebral autoregulation and anesthesia. Curr. Opin. Anaesthesiol 22, 547–552.

Dorr, A., Sled, J.G., and Kabani, N. (2007). Three-dimensional cerebral vasculature of the CBA mouse brain: a magnetic resonance imaging and micro computed tomography study. Neuroimage 35, 1409–1423.

Fouquet, J.P., Lebel, R., Cahill, L.S., Sled, J.G., Tremblay, L., and Lepage, M. (2020). Cerebrovascular MRI in the mouse without an exogenous contrast agent. Magn. Reson. Med. 84, 405–415.

Ghanavati, S., Yu, L.X., Lerch, J.P., and Sled, J.G. (2014). A perfusion procedure for imaging of the mouse cerebral vasculature by X-ray micro-CT. J. Neurosci. Methods 221, 70–77.

Grossberg, J.A., Howard, B.M., and Saindane, A.M. (2019). The use of contrast-enhanced, time-resolved magnetic resonance angiography in cerebrovascular pathology. Neurosurg. Focus 47, E3.

Hildebrand, M. (1968). 6-2 injection for subsequent corrosion, cleaning or clearing. In Anatomical Preparations), M. Hildebrand, ed. (University of California Press), pp. 66–70.

Hlushchuk, R., Haberthür, D., Soukup, P., Barré, S.F., Khoma, O.Z., Schittny, J., Jahromi, N.H., Bouchet, A., Engelhardt, B., and Djonov, V. (2020). Innovative high-resolution microCT imaging of animal brain vasculature. Brain Struct. Funct. 225, 2885–2895.

Hong, S.H., Herman, A.M., Stephenson, J.M., Wu, T., Bahadur, A.N., Burns, A.R., Marrelli, S.P., and Wythe, J.D. (2020). Development of barium-based low viscosity contrast agents for micro CT vascular casting: application to 3D visualization of the adult mouse cerebrovasculature. J. Neurosci. Res. 98, 312–324.

Kirst, C., Skriabine, S., Vieites-Prado, A., Topilko, T., Bertin, P., Gerschenfeld, G., Verny, F., Topilko, P., Michalski, N., Tessier-Lavigne, M., et al. (2020). Mapping the fine-scale organization and plasticity of the brain vasculature. Cell 180, 780–795.e25.

Knutsen, R.H., Gober, L.M., Sukinik, J.R., Donahue, D.R., Kronquist, E.K., Levin, M.D., McLean, S.E., and Kozel, B.A. (2020). Vascular casting of adult and early postnatal mouse lungs for micro-CT imaging. J. Vis. Exp. https://doi.org/10.3791/61242.

Lai, H.M., Liu, A., Ng, H., Goldfinger, M.H., Chau, T.W., DeFelice, J., Tilley, B.S., Wong, W.M., Wu, W., and Gentleman, S.M. (2018). Next generation histology methods for three-dimensional imaging of fresh and archival human brain tissues. Nat. Commun. 9, 1066.

Lee, K., Lai, H.M., Soerensen, M.H., Hui, E.S., Ma, V.W., Cho, W.C., Ho, Y.S., and Chang, R.C. (2021). Optimised tissue clearing minimises distortion and destruction during tissue delipidation. Neuropathol. Appl. Neurobiol. 47, 441–453.

Liao, F.F., Lin, G., Chen, X., Chen, L., Zheng, W., Raghow, R., Zhou, F.M., Shih, A.Y., and Tan, X.L. (2021). Endothelial nitric oxide synthase-deficient mice: a model of spontaneous cerebral small-vessel disease. Am. J. Pathol. 191, 1932–1945.

Merill, L.K. (1940). Vinylite resins, new plastic molding materials. Chem. Eng. News 18, 496–497.

Merlini, M., Shi, Y., Keller, S., Savarese, G., Akhmedov, A., Derungs, R., Spescha, R.D., Kulic, L., Nitsch, R.M., Lüscher, T.F., et al. (2017). Reduced nitric oxide bioavailability mediates cerebroarterial dysfunction independent of cerebral amyloid angiopathy in a mouse model of Alzheimer's disease. Am. J. Physiol. Heart Circ. Physiol. 312, H232–H238.

Micro Photonics. (2016). Ex vivo staining of embryos (mouse) with phospho-tungstic acid for soft tissue contrast in micro-CT imaging .https://www.microphotonics.com/assets/base/doc/embryostainingwithPTAforexvivomicro-ctimaging.pdf.

Pastor, G., Jiménez-González, M., Plaza-García, S., Beraza, M., Padro, D., Ramos-Cabrer, P., and Reese, T. (2017). A general protocol of ultra-high resolution MR angiography to image the cerebro-vasculature in 6 different rats strains at high field. J. Neurosci. Methods 289, 75–84.

Quintarelli, G., Cifonelli, J.A., and Zito, R. (1971). On phosphotungstic acid staining. II. J. Histochem. Cytochem. 19, 648–653.

Renier, N., Wu, Z., Simon, D.J., Yang, J., Ariel, P., and Tessier-Lavigne, M. (2014). iDISCO: a simple, rapid method to immunolabel large tissue samples for volume imaging. Cell 159, 896–910.

Rindone, A.N., Liu, X., Farhat, S., Perdomo-Pantoja, A., Witham, T.F., Coutu, D.L., Wan, M., and Grayson, W.L. (2021). Quantitative 3D imaging of the cranial microvascular environment at single-cell resolution. Nat. Commun. 12, 6219.

Rosenblum, J.S., Cappadona, A.J., Argersinger, D.P., Pang, Y., Wang, H., Nazari, M.A., Munasinghe, J.P., Donahue, D.R., Jha, A., Smirniotopoulos, J.G., et al. (2020). Neuraxial dysraphism in EPAS1-associated syndrome due to improper mesenchymal transition. Neurol. Genet. 6, e414.

Rosenblum, J.S., Wang, H., Dmitriev, P.M., Cappadona, A.J., Mastorakos, P., Xu, C., Jha, A., Edwards, N., Donahue, D.R., Munasinghe, J., et al. (2021). Developmental vascular malformations in EPAS1-gain-of-function syndrome. JCI Insight 6, e144368.

Slupe, A.M., and Kirsch, J.R. (2018). Effects of anesthesia on cerebral blood flow, metabolism, and neuroprotection. J. Cereb. Blood Flow Metab. 38, 2192–2208.

Tang, J., Postnov, D.D., Kilic, K., Erdener, S.E., Lee, B., Giblin, J.T., Szabo, T.L., and Boas, D.A. (2020). Functional ultrasound speckle decorrelation-based velocimetry of the brain. Adv. Sci. 7, 2001044.

Venturelli, M., Pedrinolla, A., Galazzo, I.B., Fonte, C., Smania, N., Tamburin, S., Muti, E., Crispoltoni, L., Stabile, A., Pistilli, A., et al. (2018). Impact of nitric oxide bioavailability on the progressive cerebral and peripheral circulatory impairments during aging and alzheimer's disease. Front. Physiol. 9, 169.

Vogelstein, J.T., Perlman, E., Falk, B., Baden, A., Roncal, W.G., Chandrashekhar, V., Collman, F., Seshamani, S., Patsolic, J.L., Lillaney, K., et al. (2018). A community-developed open-source computational ecosystem for big neuro data. Nat. Methods 15, 846–847.

Walker, E.J., Shen, F., Young, W.L., and Su, H. (2011). Cerebrovascular casting of the adult mouse for 3D imaging and morphological analysis. J. Vis. Exp. 57, e2958.

Wang, H., Cui, J., Yang, C., Rosenblum, J.S., Zhang, Q., Song, Q., Pang, Y., Fang, F., Sun, M., Dmitriev, P., et al. (2019). A transgenic mouse model of Pacak-Zhuang syndrome with an Epas1 gain-of-function mutation. Cancers (Basel) 11, 667.

Wang, Q., Ding, S.-L., Li, Y., Royall, J., Feng, D., Lesnar, P., Graddis, N., Naeemi, M., Facer, B., and Ho, A. (2020). The allen mouse brain common coordinate framework: a 3D reference atlas. Cell 181, 936–953.e20.

Xiong, B., Li, A., Lou, Y., Chen, S., Long, B., Peng, J., Yang, Z., Xu, T., Yang, X., Li, X., et al. (2017). Precise cerebral vascular atlas in stereotaxic coordinates of whole mouse brain. Front. Neuroanat. 11, 128.

Cell Reports Methods
Report

STAR★METHODS

KEY RESOURCES TABLE

REAGENT or RESOURCE	SOURCE	IDENTIFIER
Chemicals, peptides, and recombinant proteins		
Heparin (1000 USP Units/mL)	Hospira NDC	0409-2720-01
CO_2 tank	Robert's Oxygen Co	N/A
Sodium nitroprusside	Sigma-Aldrich	71778-25G
Phosphate-buffered saline	BioRad	#161-0780
Microfil® (polymer compound)	Flow Tech Inc.	Kit B - MV-122
Formalin	Sigma-Aldrich	HT501128
Paraformaldehyde	Sigma-Aldrich	P6148-500G
Hydrochloric acid	Sigma-Aldrich	V800203
Ethanol	Pharmco	111000200
Phosphotungstic acid	Sigma-Aldrich	P4006-25G
Experimental models: Organisms/strains		
C57/BL6 Mouse	The Jackson Laboratory	RRID:IMSR_JAX:000664
EPAS1-gain-of-function Mouse	Zhuang Laboratory at NCI, NIH	N/A
Software and algorithms		
Neurosimplicity Imaging Suite	Neurosimplicity, LLC	N/A
Other		
1 mL syringe	Becton Dickinson	309659
10 mL syringe	Becton Dickinson	303134
30-gauge needle	Becton Dickinson	305106
50 mL conical tubes	Corning	352098
7-0 silk suture	Teleflex	103-S
CeramaCut scissors 9 cm	Fine Science tools	14958-09
Ceramic coated curved forceps	Fine Science tools	11272-50
Dumont mini-forceps	Fine Science tools	11200-14
Octagon forceps straight teeth	Fine Science tools	11042-08
Straight spring scissors	Fine Science tools	15000-08
Hemostat	Fine Science tools	13013-14
Dual syringe pump	Cole Parmer	EW-74900-10
Gauze	Covidien	441215
Induction chamber	N/A	N/A
Kimwipe	Fisher	06-666
Labeling Tape	Fisher	15966
Magnetic Base	Kanetec	N/A
Micro-CT system	Bruker	N/A
Parafilm	Bemis company, Inc.	#PM999
PE-10 tubing	Instech	BTPE-10
Steel Plate	N/A	N/A
Surgical Board	Fisher	12-587-20
Zeiss Stemi-508 Dissection Scope	Zeiss	N/A

RESOURCE AVAILABILITY

Lead contact
Further information and requests for resources and reagents should be directed to and will be fulfilled by the lead contact, Jared S. Rosenblum (jared.rosenblum@nih.gov).

Materials availability
This study did not generate new unique reagents.

Data and code availability
This paper does not report Standardized datatypes. All data reported in this paper will be shared by the lead contact upon request.
  This paper does not report original code.
  Any additional information required to reanalyze the data reported in this paper is available from the lead contact upon request.

EXPERIMENTAL MODEL AND SUBJECT DETAILS

Animals
Mice were maintained under standard conditions approved by the Institutional Animal Care and Use Committee (IACUC) of *Eunice Kennedy Shriver* National Institute of Child Health and Human Development. Animals were housed in a specific pathogen–free animal house under a 12/12-hour light/dark cycle and were provided food and water ad libitum. A mouse model of the *EPAS1 gain-of-function* mutation syndrome, Pacak-Zhuang syndrome, bearing the *Epas1*A529V mutation was established in our lab as previously described (Wang et al., 2019). Briefly, a conditional knock-in Epas1neo mouse line (B6:129 mixed background) was established by TALEN-mediated homologous recombination. E2a-Cre transgenic mice with B6 background were kindly provided by Alex Grinberg of *Eunice Kennedy Shriver* National Institute of Child Health and Human Development. We obtained the mutant mice (E2a-Cre; EPAS1neo/+, in brief, *Epas1*A529V) by breeding *Epas1*neo mice with E2a-Cre transgenic mice. Littermate control mice or age matched C57BL/6J wild type mice (Jackson Laboratories RRID:IMSR_JAX:000664) were used for all experiments. Adult (5 months) male and female mice were used for all experimental testing. For wild type mice, three males and three females were used. For the mutant mice, we used four males and two females.

METHOD DETAILS

Vascular perfusion and casting
Mice were given an intraperitoneal injection of heparin (1 unit/g) and allowed to ambulate for 2 minutes prior to euthanasia via carbon dioxide narcosis, laparotomy, and bilateral thoracotomy as follows with a success rate of 100% of the 12 mice in this study. Successful euthanasia was confirmed by lack of reflexive withdrawal on paw pinch maneuver. The mice were positioned supine on a surgical board and all four limbs were secured. A midline incision through the abdominal wall was made and the xyphoid process was secured with a hemostat. Note, if greater exposure is needed to cannulate the aorta, the diaphragm can be taken down and the rib cage can be incised bilaterally inferior to the internal thoracic arteries to allow elevation of the anterior chest wall and exposure of the thoracic arteries. However, the aorta and inferior vena cava can be accessed from the abdominal cavity. The inferior vena cava (IVC) was identified and secured with a 7-0 silk suture (Teleflex, Coventry, CT), referred to as suture below; a second suture was loosely placed around the IVC and a small incision was made in the IVC between the distal and proximal suture. A segment of the exposed abdominal or thoracic descending aorta was isolated and two loose sutures were placed around it; a small opening was distal to those sutures.

  The appropriate solutions for flushing blood from the vascular system, dilating the vasculature, and casting the vessels were prepared as follows. A 10 milliliter (mL) syringe was filled with 10^{-4} M sodium nitroprusside (Sigma, St. Louis, MO) in phosphate-buffered saline (PBS) and connected to a 30-gauge (30G) needle (Beckton Dickinson, Franklin Lakes, NJ), which was then fastened to a custom catheter comprised of a 15-centimeter (cm) length of polyethylene-10 (PE-10) tubing (Instech, Plymouth Meeting, PA). This catheter was flushed to expel all air bubbles from the tubing and syringe. The PE-10 catheter was inserted into the aorta via the previously made incision and advanced beyond the sutures, which were then secured. A mixture of Microfil® polymer (Flowtech Inc, Carver, MA) in a 2:7:1 ratio of Microfil®:diluent:polymerizing agent, which was optimized to allow for arteriovenous transit and visualization on Micro-CT, was prepared in 5 mL syringes as needed and used immediately after preparation to avoid curing prior to perfusion.

  The mice were then perfused and casted as follows, which was successful in 10 of 12 mice in this study (83%). Sodium nitroprusside was perfused to remove blood from and maximally dilate vasculature; this was continued until the perfusate exiting the IVC ran clear. The catheter was left in place. The syringe containing the polymer mixture was purged of air and connected to the catheter to avoid the introduction of air bubbles into the vasculature. The polymer mixture was slowly perfused into the vasculature until it could be seen exiting the IVC; the suture was then secured around the IVC to stop the polymer outflow. The mouse was then placed in the prone position, and the scalp was then tented and incised midline from the snout to the neck to expose the skull and preserve the

Galea, which is highly vascularized. This allows visualization of the dural venous sinuses and diploic veins, which can be seen through the thin murine skull. Diploic veins will have occasional areas of redness where blood was incompletely flushed through these small channels. The polymer mixture perfusion is continued until all visible vessels and sinuses are filled. Note, while incising the Galea does allow better visualization of the diploic veins, it may lead to small vessel leaks and decreased perfusion pressure. This can lead to incomplete filling.

Following complete casting, the mice are cured and fixed, which was successful in 12/12 (100%) of mice in this study. The polymer in sample was cured for approximately 60-90 minutes. Depending on downstream applications, the sample may be cured on ice, dry ice, or at 4°C to prevent tissue decay. Note, we placed our samples on a cardboard barrier in a container of dry ice to avoid direct contact with the dry ice, which prevents rapid water crystal formation. Water crystals can create artifacts in histologic processing. The samples were fixed for 36 hours using a fixative most suitable for downstream applications. We used 4% paraformaldehyde (PFA) for 36 hours at 4°C when immunohistochemistry was anticipated. When only cytomorphologic assessment was anticipated, the samples were fixed in 10% formalin for 24 hours. When immunohistochemistry needs to be performed on a formalin fixed sample that has been sectioned, antigen retrieval can be performed. The samples were then transferred into phosphate-buffered saline and stored in 4°C until imaging.

Iterative sample processing and micro-CT image acquisition

The samples were then imaged via iteratively processed and imaged via Micro-CT to obtain images of bone, soft tissues, and vessels, which was successful in 12 of 12 (100%) of mice in this study. We acquired images using both the SkyScan 1172 and 1272 Micro-CT scanner (Bruker microCT, Kontich, Belgium). Other micro-CT instruments may be used; the instrument should be capable of multi-segment scanning and have a variety of filter materials and thicknesses. The samples were secured to prevent changes in hydration and movement using a holder sized appropriately to fit within scanner field of view (FOV). We determined the optimal scanning parameters for each sample and acquired a bright field prior to each scan. Settings for each iterative scan can be found in Table S1. Following each scan, the sample was stored in phosphate-buffered saline.

Acquired images were reconstructed and visualized using Bruker (Billerica, Massachusetts, U.S.) software including NRecon, Dataviewer, and CTVox. The dynamic range was adjusted such that the signal of most dense material, usually enamel, was at the upper limit. Ring artifact reduction and beam hardening correction were applied. Note, if performing analysis on multiple samples, keep the dynamic range and beam hardening correction, the same between samples. The acquired image orientation can be rotated in Data-Viewer. Volume rendered 3D images can be generated and viewed using CTVox or any other software capable of viewing the image files.

The acquired images from the initial scan following vascular casting contain bone and casted vessels with high radiodensity. To separate bone from vessels, the samples were decalcified in a solution of 10% hydrochloric acid for 3-5 at room temperature with agitation days before acquisition of a second Micro-CT scan, which makes bone radiolucent. Note, a weak acid decalcification can be performed but the timing will vary for optimal radiolucency. Following decalcification, the sample was rinsed with deionized water and stored in phosphate-buffered saline before acquisition of the second Micro-CT scan, which revealed the casted vessels alone.

To visualize soft tissue, bone, and vessels, we immersed the samples in a 1:40 volume/volume solution phosphotungstic acid (PTA) in 70% ethanol following a graded ethanol dehydration comprised of sequential overnight immersion in 30%, 50%, and 70% ethanol, all of which takes between 8 to 10 days (Micro Photonics, 2016). To determine adequate diffusion of PTA to the center of sample, we performed a scout Micro-CT scan at low resolution. If the low-resolution scout scan displayed incomplete diffusion of PTA, which is seen as low or absent attenuation of soft tissue of the brain in the center of the sample, we returned the sample to the PTA/ethanol solution for several days and then repeated the low-resolution scout scan.

Optimizing micro-CT parameters

Optimal transmission occurs when X-Ray absorption through each material in the field of view has unique radiodensity without saturation (maximum absorption or transmission) as shown in Figure S1. To delineate the smallest feature of interest within the sample, a minimum of 2-4 pixels/voxels are needed. Low spatial resolution can limit visualization of small features of interest; more pixels/voxels will increase resolution of smaller features. Improper tuning of the X-ray settings, exposure time, and power settings can result in artifacts in the image. An appropriate filter needs to be applied relative to the accelerating voltage (kV) and radiodensity of the sample to tune out the lower kV spectrum and allow the higher kV spectrum. Higher atomic density materials require higher accelerating voltages. More radiodense samples require thicker filters. In our case, aluminum is thinner (less filtration) than copper (more filtration). X-ray settings, exposure time, and power settings need to be optimized to have sufficient transmission through the sample to resolve the Microfil, bone, PTA per the above criteria. Our workflow can be done on any Micro-CT machine so long as these principles are followed.

Micro-CT images were visualized and rendered in 3D using the Bruker software suite, including SkyScan CTVox.

Image processing

We used the Neurosimplicity Imaging Suite (Neurosimplicity, LLC NJ, USA), which leverages and combines automatic deformable registration such as CloudReg, an open source tool (Chandrashekhar et al., 2021), with automatic segmentation/feature extraction, and visualization, such as some available open source visualization tools (Vogelstein et al., 2018), to register the iteratively processed

and imaged Micro-CT samples to each other and to an atlas such as the ARA CCFv3, extract features of interest, and visualize the resulting registered two-dimensional (2D) raw data and three-dimensional (3D) data. Image processing steps including 1) denoising with a Gaussian kernel, 2) binary thresholding, 3) morphological operations were applied to the raw 2D data to generate the segmentations. This software can handle raw data files including bitmap, TIF, and DICOM. Micro-CT images were also viewed in the Bruker software suite, including SkyScan CTVox (Micro Photonics, Inc.)

Troubleshooting
Procedural step: Perfusion
Problem 1. Nitroprusside and/or Microfil® are leaking from cannulation site.
Possible reasons. (1) The needle may not extend beyond sutures. (2) The sutures securing the needle may be too loose. (3) The walls of the aorta may be damaged, either from tight suture or improper cannulation.
Solutions. (1) Recannulate and/or adjust the needle. (2) Tighten the sutures tied around the aorta. Do not transect the aorta. (3) Recannulate proximal to the current cannulation site.
Problem 2. Microfil® is extravasating, but not exiting from the IVC.
Possible reasons. (1) The internal thoracic arteries may have been damaged during thoracotomy. (2) A vessel may have ruptured due to high perfusion pressure.
Solutions. (1) Avoid elevating the chest. Cannulate the abdominal aorta. (2) Prepare a new sample. Perfuse slowly and at a constant rate; utilize an automated syringe pump if available. Decrease viscosity of the Microfil® if problem persists.
Problem 3. There is resistance in the syringe during the Microfil® perfusion, but the endpoint has not yet been reached.
Possible reasons. (1) The Microfil® mixture may be too viscous. (2) Incomplete flushing led to coagulation of blood in smaller vessels. (3) Microfil® will begin to cure within 30 minutes of preparation. Partially cured Microfil® within the syringe, catheter tubing, or some vessels may be restricting further perfusion.
Solutions. (1) Prepare a new sample. Check that the ratio of the Microfil® mixture is correct; optimize as needed. (2) Prepare a new sample. Flush with nitroprusside promptly after euthanasia. (3) Prepare a new sample. If the sample is precious and cannot be discarded, remove catheter the catheter and place a new one; use a new syringe and mix new Microfil® solution.
Procedural step: Curation
Problem 1. The sample froze while curing.
Possible reasons. (1) Too much dry ice was used or a barrier between dry ice and the sample was not placed.
Solutions. (1) Use wet ice, or less dry ice. Do not put samples directly on the ice. The sample should be fine; proceed to fixation.
Problem 2. Uncured Microfil® is floating in the fixative solution.
Possible reasons. (1) Inadequate curation. Altering the viscosity may require longer curation time.
Solutions. (1) Cure for an additional 60 minutes for a total of 120 minutes of curation. If Microfil® extravasated during curation, prepare a new sample and repeat protocol.
Procedural step: Visualization
Problem 1. The scans look blurry.
Possible reasons. (1) The sample may have shifted during the scan. (2) If the sample was still cold at the start of the scan, movement may have occurred during the scan as the sample thawed. (3) Sample may have dried out. Fluid loss in soft tissues, especially during long scans, can cause the sample to shift.
Solutions. (1) Fill gaps in the sample tube with Styrofoam of other radiolucent material to secure sample. (2) Rescan the sample. Allow the samples to warm to room temperature prior to scanning. (3) Wrap the sample in parafilm to maintain the moisture content. Adjust parameters to decrease scan time.
Problem 2. It is difficult to distinguish Microfil® from bone.
Possible reasons. (1) Micro-CT parameters were not optimized. (2) 3D reconstruction parameters were not optimized. (3) Scans were output in 8-bit. (4) Decalcification was not performed. (5) Air bubbles may have entered the vascular system.
Solutions. (1) Optimize scan parameters, including the X-ray power and filter type/thickness. (2) Adjust the dynamic range. The upper limit should be just above the densest signal (typically enamel). The lower limit is generally zero. (3) Alternatively, increasing the lower limit and decreasing the upper limit will remove soft tissue from the scan and saturate bone signal; this may make it easier to segment the Microfil® density. (4) Output the data in 16-bit format. This may allow for easier segmentation of the Microfil® signal. (5) Perform an acid immersion to decalcify bone.
Problem 3. Micro-CT shows inconsistent perfusion or gaps in Microfil® signal, especially in smaller vessels.
Possible reasons. (1) Air bubbles may have entered the vascular system. (2) The transfer function has not been optimized. (3) Incomplete flushing led to coagulation of blood in smaller vessels. (4) Microfil® will begin to cure within 30 minutes of preparation. Partially cured Microfil® within some vessels may have prevented complete perfusion. (5) Not enough Microfil® was injected into the sample.
Solutions. (1) Prepare a new sample. Flush the catheter and make certain there are no air bubbles in either tubing or syringe during nitroprusside and Microfil® perfusion. (2) Adjust the transfer function to identify only the threshold range associated with smaller vessels. Note, visualization of these vessels may result in increased background noise. (3) Prepare a new sample. Flush with nitroprusside completely, until perfusate exiting the IVC is clear. (4) Prepare a new sample. Perfuse at a constant rate. Use of an automatic

syringe pump may be desired. (5) The exact volume of perfused Microfil® will vary from sample to sample. Continue injecting until Microfil® is seen exiting the IVC.

Problem 4. There is hematoma at the posterior aspect of the head, as well as broken bones.

Possible reasons. (1) Methods of euthanasia that inflict physical trauma, particularly cervical dislocation, can damage anatomy.

Solutions. (1) Euthanasia via carbon dioxide narcosis and laparotomy/bilateral thoracotomy.

Problem 5. Only arteries and/or only large vessels can be seen.

Possible reasons. (1) The Microfil® mixture may have been too viscous.

Solutions. (1) Check the ratio of Microfil®:diluent:polymerizing agent; we found that a ratio of 2:7:1 crosses capillaries. Optimize this ratio as needed.

QUANTIFICATION AND STATISTICAL ANALYSIS

We quantified and analyzed basilar artery length and diameter for its 3 main segments as defined in Table S2. We took these measurements for 5 wild-type and 5 mutant (*EPAS1 gain-of-function*) mice. Means and standard deviations were computed within groups and for each measurement taken. More information is available in Table S2.